

Reduction Algorithms for the Multiband Imaging Photometer for Spitzer: 6 Months of Flight Data

K. D. Gordon, C. W. Engelbracht, J. Muzerolle, J. A. Stansberry, K. A. Misselt, J. E. Morrison, G. Rieke, J. Cadien, E. T. Young, H. Dole, D. M. Kelly, A. Alonso-Herrero, E. Egami, K. Y. L. Su, C. Papovich, P. S. Smith, D. C. Hines, M. J. Rieke, M. Blaylock, P. G. Pérez-González, E. Le Floc'h, J. Hinz

Steward Observatory, University of Arizona, Tucson, AZ, 85721, USA

and

W. B. Latter, T. Hesselroth, D. T. Frayer, A. Noriega-Crespo, F. J. Masci, D. L. Padgett
Spitzer Science Center, Pasadena, CA, 91125, USA

ABSTRACT

The first six months of flight data from the Multiband Imaging Photometer for Spitzer (MIPS) were used to test MIPS reduction algorithms based on extensive preflight laboratory data and modeling. The underlying approach for the preflight algorithms has been found to be sound, but some modifications have improved the performance. The main changes are scan mirror dependent flat fields at 24 μm , hand processing to remove the time dependent stim flash latents and fast/slow response variations at 70 μm , and the use of asteroids and other sources instead of stars for flux calibration at 160 μm due to a blue “leak.” The photometric accuracy of flux measurements is currently 5%, 10%, and 20% at 24, 70, and 160 μm , respectively. These numbers are expected to improve as more flight data are analyzed and data reduction algorithms refined.

1. INTRODUCTION

The Multiband Imaging Photometer for Spitzer (MIPS) provides the far-infrared capabilities for the Spitzer Space Telescope. MIPS provides images at 24, 70, and 160 μm with well sampled point-spread-functions. In addition, low resolution spectra from 52 to 100 μm can be obtained using the Spectral Energy Distribution mode. The detectors at 24, 70, and 160 μm are a 128x128 Si:As BIB array, a 32x32 Ge:Ga array, and a 20x2 stressed Ge:Ga array. The MIPS instrument is described by Rieke et al.¹ and Rieke et al.² and the Spitzer Space Telescope by Werner et al.³ The reduction of MIPS data is the subject of this paper, specifically the modifications needed to preflight algorithms⁴ after analysis of the first six months of flight data. As the analysis of flight data is ongoing, this paper is necessarily a progress report.

2. SUMMARY OF PREFLIGHT REDUCTION ALGORITHMS

Extensive efforts before the launch of Spitzer were made to prepare reduction algorithms for all three MIPS arrays. The results of this work are presented by Gordon et al.⁴ and summarized in this section.

Figure 1 gives a pictorial representation of the preflight algorithms split into three stages. The first stage (“Ramps to Slopes”) transforms the non-destructive samples in an integration ramp into a slope measurement while performing corrections with time scales on order of the exposure time. The second stage (“Slope Calibration”) calibrates the raw slopes to remove instrumental effects with time scales longer than an individual exposure time. Finally, the third stage (“Redundancy”) takes a set of exposures and combines them into a single mosaicked image while correcting for optical distortions and rejecting outliers. This third stage was the hardest to define fully with only preflight data, especially how to make full use of the redundancy in the data-taking to improve the removal of instrument signatures and data artifacts.

Send correspondence to K. D. Gordon, Email: kgordon@as.arizona.edu

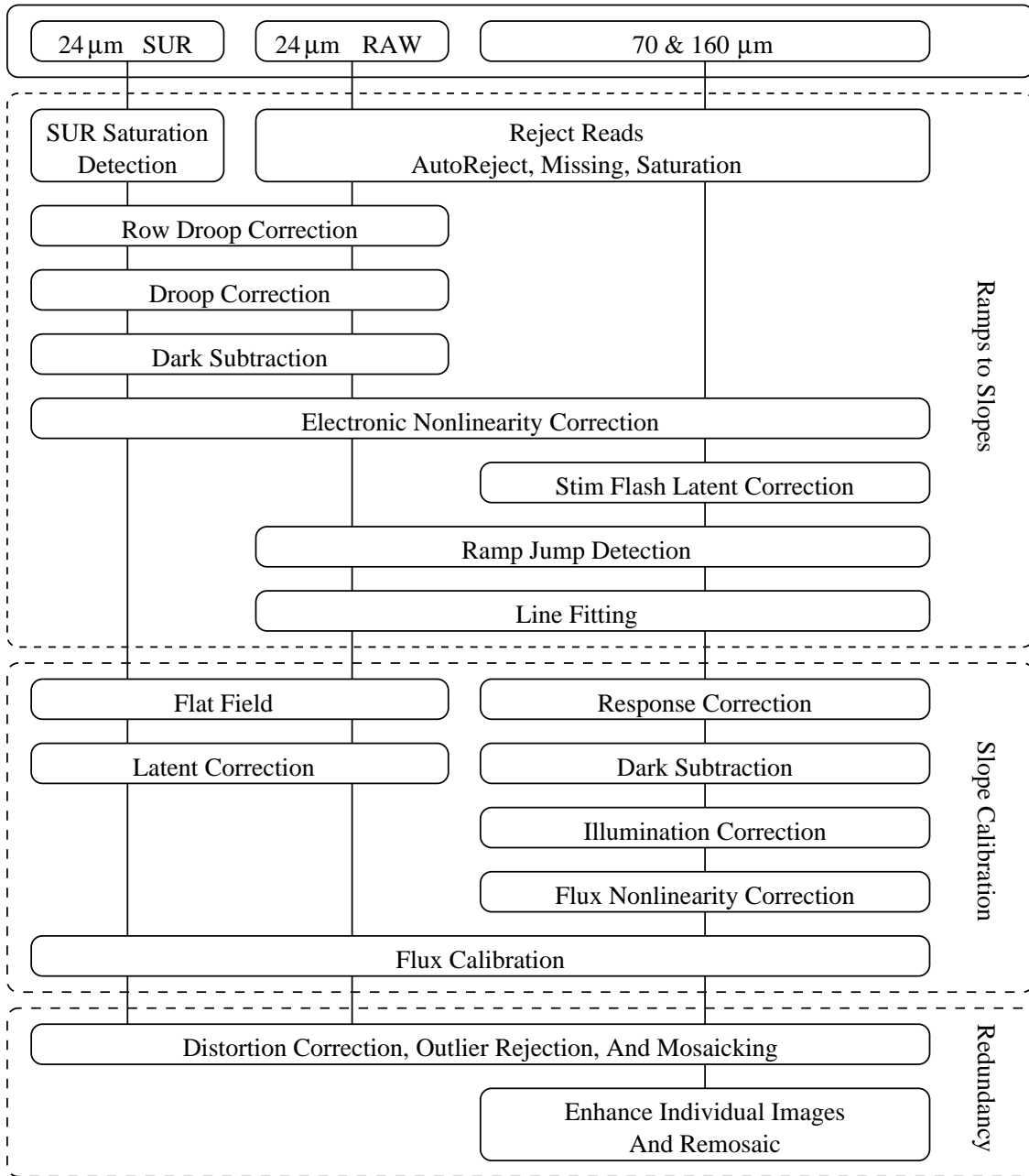


Figure 1. Graphical representations of the flow of reduction of MIPS data based on preflight expectations.

All three arrays are non-destructively read out continuously at intervals of either 1/2 or 1/8 of a second for the 24 and 70/160 μm arrays, respectively. After the exposure is complete, the arrays are reset and the charge starts building up again. The majority of 24 μm flight data is taken in sample-up-the-ramp (SUR) mode, to limit the total amount of data that must be stored on-board the spacecraft. In this mode, a slope is fit onboard Spitzer and the resulting slope measurement downlinked. In addition, the difference between the first two reads (1st difference) is also downlinked to increase the dynamic range. Some 24 μm engineering data and all 70 and 160 μm data are taken in RAW mode, under which all the non-destructive reads are downlinked. In these cases, the basic unit of data is a well-sampled charge accumulation ramp, and slopes are fitted on the ground after preliminary processing steps such as rejecting invalid data and making linearity corrections.

While the three MIPS arrays share some reduction steps, there is a natural division between the reduction of the Si:As 24 μm array data and that from the Ge:Ga 70 and 160 μm arrays.

For 24 μm SUR mode data, the first step in the “Ramps to Slopes” stage is the detection of saturation, which is done by comparing the slope and 1st difference values. Next, row droop and droop corrections are applied. Droop is an electronic effect that raises the overall output level of the whole array by an amount proportional to the total charge on the array. Row droop is similar but only applies along rows. The very small dark signal is subtracted and nonlinearities (up to 14%) due to the electronics corrected based only on the overall slope. When 24 μm RAW mode data are reduced, similar steps are applied but on the full ramp data instead of the slopes. In addition, having the ramp means that saturation detection is cleaner and cosmic rays (ramp jumps) can be detected and removed. The final step is then fitting the ramp to produce the slope measurement. The remaining steps are identical for both SUR and RAW mode data. In the “Slope Calibration” stage, the flat field is applied, source latent images are corrected and the flux calibration applied. Finally, the “Redundancy” stage creates the final mosaics after correcting for distortions and rejecting outliers.

For the 70 and 160 μm data, the first step in the “Ramps to Slopes” stage is to reject bad reads in the charge ramps. These bad reads can be due to reset pulse transients (autoreject), missing data, or saturation. Next, the small (1-2%) electronic nonlinearities are corrected and the stim flash latents removed. The stimulators are used to track the changing response of the Ge:Ga detectors and are flashed about every two minutes. These bright flashes leave latent images, but with amplitudes less than a percent or two and time constants less than 20 seconds. Next, jumps in the ramps due to cosmic rays or electronics (readout jumps) are detected. Finally, the ramp segments are fit to the valid segments of data and the slope measurement determined. The “Slope Calibration” stage starts by correcting the changing response of the detectors by dividing by the stim flashes. The dark, also calibrated by dividing by the stim flashes, is subtracted. The illumination pattern of the telescope/instrument and the stim flash is removed using an illumination correction determined using flat sky observations (like a traditional flat field). The bulk Ge:Ga photoconductors are subject to flux dependent signal nonlinearities. These effects are corrected on a pixel-by-pixel basis using extensive calibration observations. Finally, the flux calibration based on stellar observations is applied. In the “Redundancy” stage, optical distortions are removed and outliers rejected using the redundancy inherent in the basic unit of observations. Finally, the redundancy is used to search for residual instrumental signatures to remove them and then the data are remosaicked. The approaches for this final step are only now being defined, as flight data are analyzed. We anticipate that improvements will be made throughout the mission.

3. FLIGHT DATA

The preflight algorithms reflect extensive analysis of laboratory data on the flight or similar arrays and theoretical modeling of Ge:Ga detectors. Nevertheless, it was always expected that the realities of data taken in flight would require modification of these algorithms. This paper details the changes resulting from the continuing analysis of MIPS flight data during the three months of instrument commissioning data (In Orbit Checkout/Science Verification) and roughly three months of nominal science operations.

The current state of knowledge of the best MIPS data reduction algorithms is given in pictorial form in Figure. 2. The details of the modifications from Figure 1 are discussed in the following sections for each array in turn. The largest change in the reduction algorithms is the addition of a “Hand Processing” stage between the “Slope Calibration” and “Redundancy” stages. The “Hand Processing” may disappear in the future after sufficient knowledge and testing occurs to provide automatic versions of these steps.

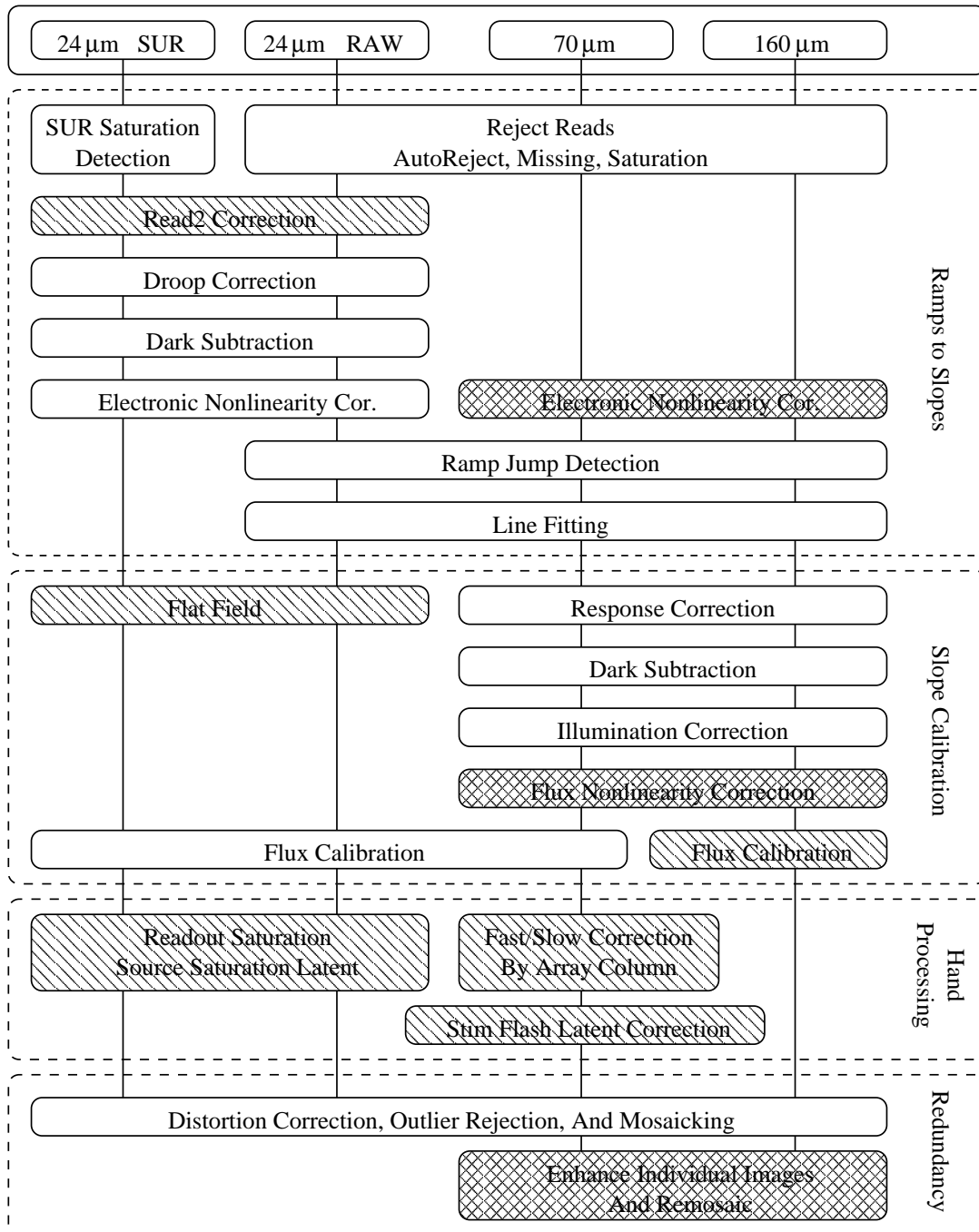


Figure 2. Graphical representations of the flow of reduction of MIPS data based on preliminary analysis of flight data. Left leaning hatching denotes steps which are significantly changed from preflight expectations and left/right hatching means steps which have not been implemented for flight data yet.

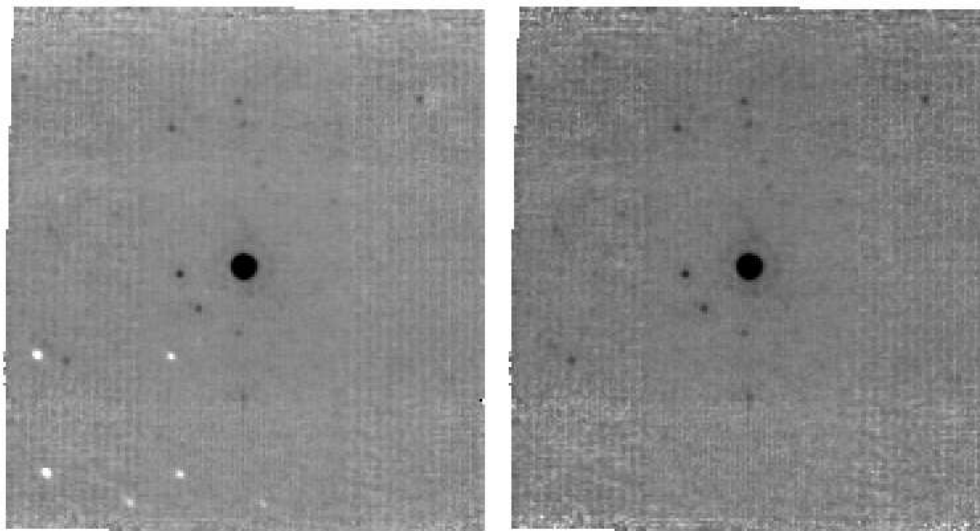


Figure 3. The importance of scan mirror dependent flats for reduction of $24\ \mu\text{m}$ data is shown. The left panel has a single scan mirror independent flat applied and the right panel has scan mirror dependent flats applied. Both panels are the result of mosaicking a set of images taken in photometry mode. Notice the four white points in a grid pattern in the left panel which are not present in the right panel. Other similar, weaker features can also be seen in the left, but not right panel.

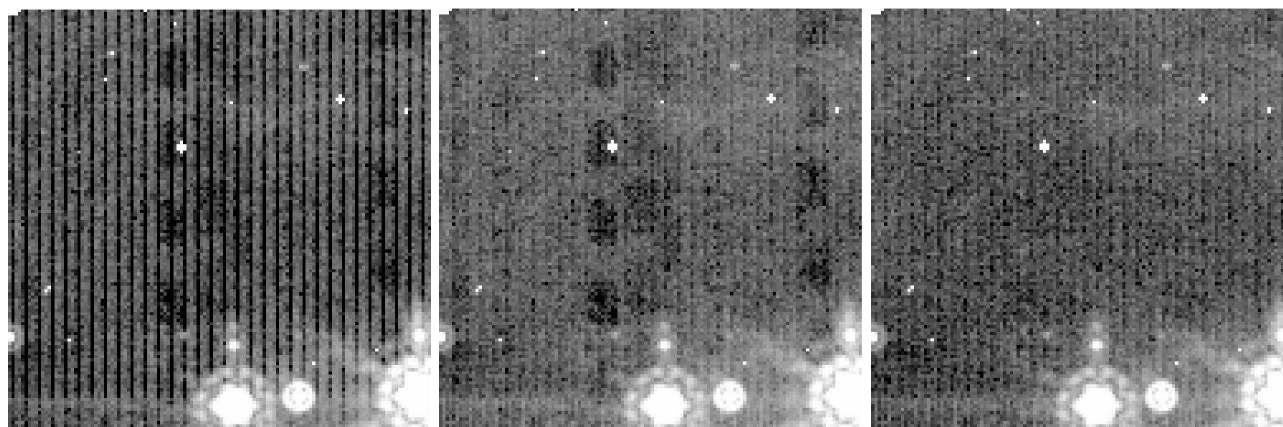


Figure 4. The readout saturation and saturating source latent are shown in the left panel. The center panel has the readout saturation correction applied. The right panel has the readout and saturation source saturations removed.

3.1. $24\ \mu\text{m}$

As expected, the $24\ \mu\text{m}$ reduction algorithms required only minor modifications to produce excellent, well calibrated $24\ \mu\text{m}$ images. The most significant change required creating flat fields for each scan mirror position used instead of a single flat field. Small particles were deposited on the pick-off mirror, probably during launch. The light they block leads to spots in the images whose positions are dependent on the scan mirror angle. By reducing the $24\ \mu\text{m}$ data with scan mirror dependent flat fields, the spots are cleanly removed as can be seen in Figure 3.

The Row Droop effect was not seen in the flight data and the correction for this effect has been removed. In the place of this step, a new correction for what is termed the “Read2” effect has been inserted. The “Read2” effect describes the bias introduced into the SUR mode slope measurement by a small additive offset to the

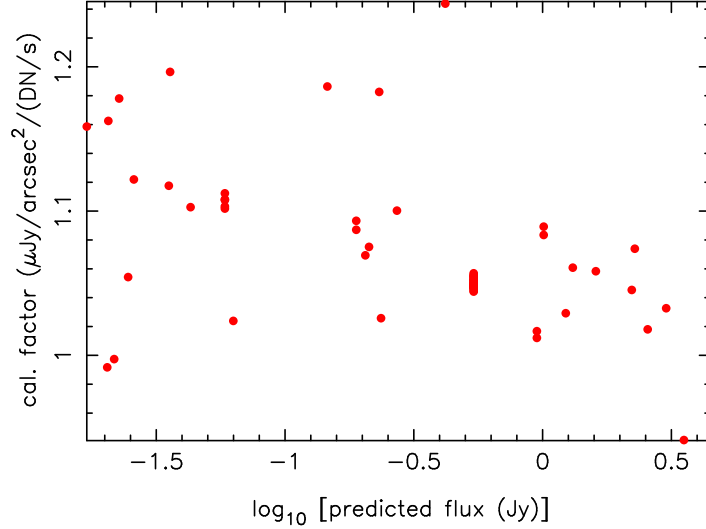


Figure 5. The $24\ \mu\text{m}$ calibration factor measured for the calibration star measurements (minus two high and two low outliers) is plotted.

second read of each $24\ \mu\text{m}$ ramp (the first read is automatically ignored due to known reset transients). This additive offset varies across the array and has been empirically calibrated using flight RAW mode data.

The Latent Correction has been removed from the “Slope Calibration” stage as the characterization of this correction has proven to be more difficult than anticipated. While such latents are not a major concern, it may be possible to reinstate this correction at a later date once enough data are accumulated to provide a good calibration.

There are two effects associated with saturation that are in the “Hand Processing” category. The first is caused by a hard saturating cosmic ray or astronomical source that suppresses the output of a single readout; it is termed readout saturation. As there are only four readouts for the $24\ \mu\text{m}$ array, this has the appearance of depressing every fourth column. The readout saturation can be corrected for most affected images by using the other three readouts to provide the correct overall level. The second is seen after a saturating object and results in a source latent appearing for many images afterwards. The long life of this latent means that it is possible to create a correction for the affected images on a case-by-case basis, but not for images which show significant complex structure.

The overall behavior of the $24\ \mu\text{m}$ array only can be described as excellent. Mosaics made from many individual images are clean with few, if any, instrumental residuals present. Photometry repeats to 1% or better and the absolute calibration is better than 5% determined using observations of solar analog, A, and K giant stars (see Figure 5).

3.2. $70\ \mu\text{m}$

The reduction of the $70\ \mu\text{m}$ data has benefited more than the other two arrays from the “Hand Processing” stage. This mainly has been the result of the discovery of significant time evolution of the stim flash latents and fast/slow response variations seen in flight data.

The operating parameters for the $70\ \mu\text{m}$ array have been changed a number of times during the first 6 months of the mission. Half of the $70\ \mu\text{m}$ array was lost due to a telescope cable failure when the cryostat vacuum shell cooled below 28K. In addition, the working half of the array was noisier than expected, mostly due to the increased hit rate from cosmic rays and in particular cosmic rays causing very large charge deposition (on-orbit hit rates are 2 - 3 times expectations). The bias voltage of the array was initially increased to attempt to overcome the higher noise levels. After extensive analysis of the first few months of data, it was found that a

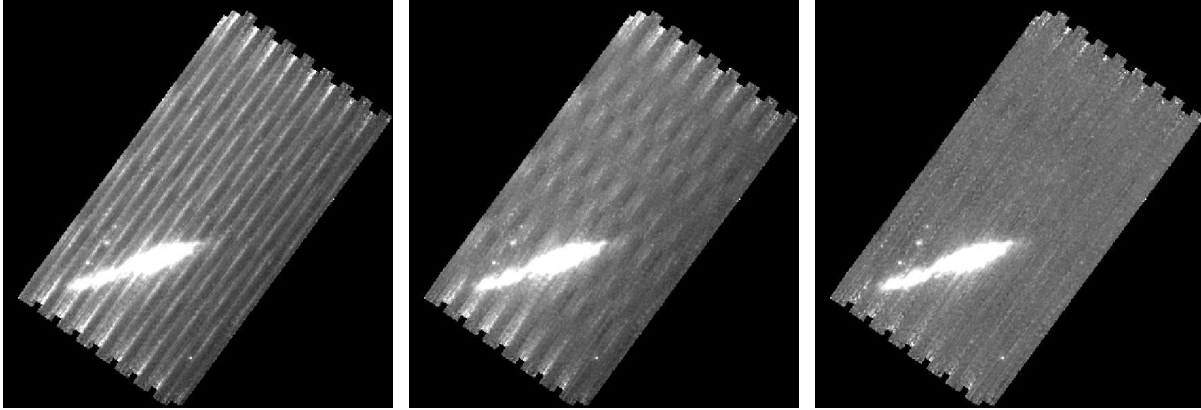


Figure 6. The scan map mode observation of NGC 55 is shown to illustrate the fast/slow response and stim flash latent temporal variations. This observation consists of 16 scan legs covering an area of 30 by 60 arcminutes and are discussed at length in Engelbracht et al.⁵ The left panel gives the scan map without the fast/slow and stim flash latent corrections. The middle panel shows the map with the fast/slow response variation correction applied. The right panel shows the final image with the stim flash latent and fast/slow response variation corrections applied.

lower array bias was better overall. Although the nominal signal-to-noise was found to be largely independent of detector bias, there were a number of undesirable effects that increased rapidly when the detector bias was raised above 45mV. They included a rapid increase in stim latent amplitudes, and a slowly changing effect on the shape of the stim latent signals. The ratio of fast to slow response also appeared to be unstable. By reducing the bias voltages to 40mV or below, these effects were reduced to the levels seen in prelaunch laboratory experiments. They are illustrated in Figure 6, data obtained with the bias set to 62mV. We discuss these effects in more detail below.

From preflight testing, it was known that the fast/slow response was time dependent at something like the 5% level. That is, the variation of the fast response as measured by the stim flashes was different from the variation of the slow response by about 5%. No correction step was formally envisioned previously, but the effect was large enough at the high array bias level to require correction. This correction is possible during the “Redundancy” stage of reduction, but for this to be possible two sets of observations are required, one which is time reversed from the other. As it has only been possible to do this for scan maps recently and not possible to do this for photometry data, the fast/slow response correction has only been possible by hand on a case-by-case basis.

The preflight expectations for stim flash latents were that they would be dependent on stim flash amplitude and background level. For routine operations, the stim flash amplitude is fixed. At the high bias setting, there was a quick time evolution of the stim flash latents from basically non-existent right after an anneal to very strong 3 hours after an anneal. This behavior is much lower, but still present, at the current lower array bias level. Given possible dependencies both on time since anneal and background level, an automatic correction may not be possible. If it is, it will require significant development and analysis of data. In the meantime, there are two possibilities for dealing with the effect. In one, a high pass filtering algorithm is used to artificially flatten the baseline, including any residuals from stim flashes. However, this approach cannot be used for extended source images, which are affected by the filter. As a result, correcting for stim flash latents on such sources is a “Hand Processing” step that is dependent on the mode (photometry versus scan map) and target (degree of source extent) of the data.

The nonlinearities in the Ge arrays are split into those caused by the electronics and those caused the detector material which are dependent on the flux level. The electronic nonlinearities were measured in preflight tests, but similar flight tests have shown some differences. As such, the electronic nonlinearity correction awaits a new calibration before being implemented. The flux nonlinearity calibration is composed of two parts. The first uses the stimulator flashed at different levels on different backgrounds to correct for the pixel-to-pixel variations in the flux nonlinearities. The second uses measurements of calibration stars to remove the global flux nonlinearities.

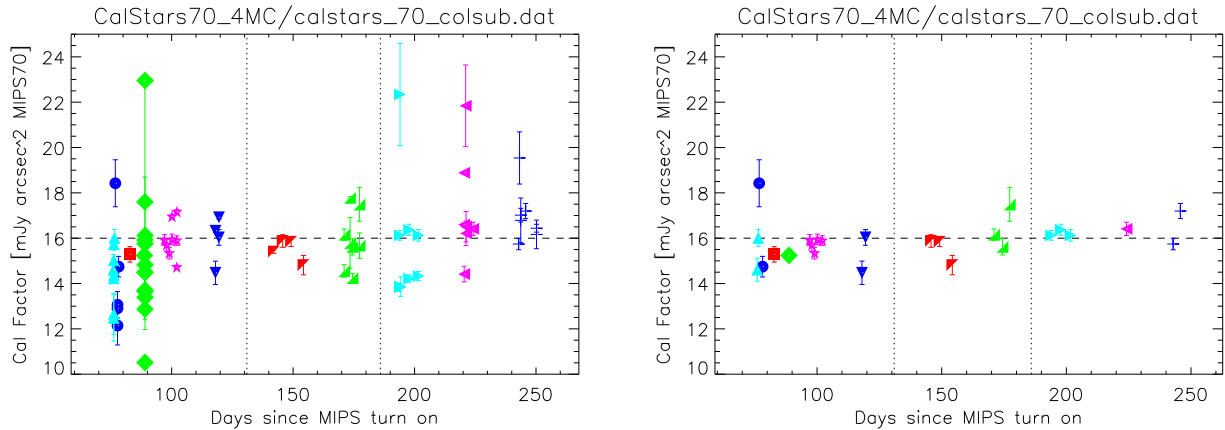


Figure 7. The $70\ \mu\text{m}$ calibration factor measured for all the calibration star measurements (left) and for just HD 163588 (right). The error bars on each point are determined from the sky noise in each individual measurement. The first vertical line denotes where the photometry mode dither pattern was changed and the second vertical line denotes where the array bias was changed from 62 to 35 mV. The horizontal line is drawn at $16\ \text{mJy arcsec}^{-2}$ (MIPS70 unit) $^{-1}$ (not the average) as a guide to the eye.

The total characterization of the flux nonlinearities is a complex process and is ongoing. As such, it has not been implemented yet.

The $70\ \mu\text{m}$ absolute calibration is based on solar analog, A, and K giant stars. Using all the calibration star measurements taken to date, the accuracy of $70\ \mu\text{m}$ measurements is around 10% (see Figure 7). These calibration measurements include stars with predicted fluxes ranging from 30 mJy to 5 Jy on backgrounds between 4 and 25 MJy/sr. One of the calibration stars (HD 163588) is measured every MIPS campaign and the repeatability of this star is better than 4%. The main difference between these two accuracies is likely the result of the nonlinearities still to be corrected.

3.3. $160\ \mu\text{m}$

The $160\ \mu\text{m}$ array is working well and the preflight reduction algorithms are effective. The largest change for $160\ \mu\text{m}$ has been the discovery in flight that this array suffers from a blue “leak” (actually an unexpected scattered reflection). For a stellar source, this “leak” is about 15 times larger than the $160\ \mu\text{m}$ stellar flux making it difficult to use stars for calibration. For sources with redder than stellar flux distributions, the leak is usually below the confusion noise.

Unlike the $70\ \mu\text{m}$ array, the $160\ \mu\text{m}$ stim flash latents are basically nonexistent after the first few seconds following the stim flash. This is different from ground test data where the stim flashes lasted long enough to warrant correction. This may be due to the lower bias in flight than in ground testing and/or the high cosmic ray rate (about 1 cosmic ray every 11 or so seconds). Thus, the stim flash latent correction step has been removed entirely for $160\ \mu\text{m}$ data.

As with the $70\ \mu\text{m}$ array, the nonlinearities at $160\ \mu\text{m}$ are not currently characterized well enough to allow correction. The electronic nonlinearities are different than seen in ground tests. The flux nonlinearities await sufficient asteroid data to allow for the global flux nonlinearities to be calibrated.

Unlike the other two MIPS arrays, the calibration of the $160\ \mu\text{m}$ data is based on a variety of measurements that include asteroids, cold sources that are well-measured by other space missions (ISO, COBE), and objects where an accurate flux level can be determined by interpolation and modeling such as stellar debris disks. The resulting multiple calibrations agree to within 20%. However, given that these were not the planned calibration sources, the $160\ \mu\text{m}$ flux calibration is currently more uncertain than for the other two MIPS arrays. Improvements in the calibration will depend largely on measurements of asteroids. The modeling of asteroids is more

involved than that of stars. To constrain models, each asteroid is observed at both 70 and 160 μm and the 70 μm measurement is entered as a constraint in the modeling. The accuracy of the 160 μm calibration is expected to improve significantly as more asteroids are observed and the modeling is improved.

ACKNOWLEDGMENTS

This work was supported by NASA JPL contract 960785.

REFERENCES

1. G. H. Rieke, E. T. Young, C. W. Engelbracht, D. M. Kelly, F. J. Low, E. E. Haller, J. W. Beeman, K. D. Gordon, J. A. Stansberry, K. A. Misselt, J. Cadien, J. E. Morrison, W. B. Latter, A. Noriega-Crespo, D. L. Padgett, K. R. Stapelfeldt, D. C. Hines, E. Egami, J. Muzerolle, A. Alonso-Herrero, M. Blaylock, H. Dole, J. L. Hinz, E. L. Floc'h, C. Papovich, P. G. Perez-Gonzalez, P. S. Smith, K. Y. L. Su, L. Bennett, D. T. Frayer, D. Henderson, N. Lu, F. Masci, M. Pesenson, L. Rebull, J. Rho, J. Keene, S. Stolovy, S. Wachter, W. Wheaton, and P. L. Richards, "The multiband imaging photometer for spitzer," *Astrophysical Journal Supplement* **in press**, 2004.
2. G. H. Rieke and et al., "The multiband imaging photometer for spitzer," *SPIE Proceedings* **this volume**, 2004.
3. M. Werner, T. Roellig, F. Low, G. Rieke, M. Rieke, W. Hoffmann, E. Young, J. Houck, B. Brandl, G. Fazio, J. Hora, R. Gehrz, G. Helou, B. Soifer, J. Stauffer, J. Keene, P. Eisenhardt, D. Gallagher, T. Gautier, W. Irace, C. Lawrence, L. Simmons, J. V. Cleve, M. Jura, and E. W. and, "The spitzer space telescope mission," *Astrophysical Journal Supplement* **in press**, 2004.
4. K. D. Gordon, G. H. Rieke, C. W. Engelbracht, J. Muzerolle, J. A. Stansberry, K. A. Misselt, J. E. Morrison, J. Cadien, E. T. Young, H. Dole, D. M. Kelly, E. E. A. Alonso-Herrero, K. Y. L. Su, C. Papovich, P. S. Smith, M. J. R. D. C. Hines, M. Blaylock, W. B. Latter, T. Hesselroth, D. T. Frayer, A. Noriega-Crespo, F. J. Masci, D. L. Padgett, M. P. Smylie, and N. M. Haegel, "Reduction algorithms for the multiband imaging photometer for spitzer," *Pub. Astron. Society Pacific* **submitted**, 2004.
5. C. W. Engelbracht, K. D. Gordon, G. J. Bendo, P. G. Perez-Gonzalez, K. A. Misselt, G. H. Rieke, E. T. Young, D. C. Hines, D. M. Kelly, J. A. Stansberry, C. Papovich, J. E. Morrison, E. Egami, K. Y. L. Su, J. Muzerolle, H. Dole, A. Alonso-Herrero, J. L. Hinz, P. S. Smith, W. B. Latter, A. Noriega-Crespo, D. L. Padgett, J. Rho, D. T. Frayer, and S. Wachter, "Far infrared imaging of ngc 55," *Astrophysical Journal Supplement* **in press**, 2004.